ADVANCED OPTICAL MATERIALS
www.advopticalmat.de

Dielectric Metasurface from Solution-Phase Epitaxy of ZnO Nanorods for Subtractive Color Filter Application

Hongjun Liu, Dunhang Quan, Ke Li, Yini Zheng, Fei Lou, Song Liu, Yanjun Liu, Abhishek Kumar Srivastava, Guixin Li, Chengfeng Qiu, Zhaojun Liu, and Xing Cheng**

In recent years, metasurfaces have received considerable attention owing to their versatile range of applications. However, in the case of metal-oxide-based dielectric metasurfaces, the difficulty and cost of a conventional top-down nano-fabrication process largely hinder their applications. In this work, a fabrication method is proposed for dielectric metasurfaces based on the solution-phase epitaxy of ZnO nanorods. Using this method, precise control of the size and position of the synthesized ZnO nanostructures is achieved. Furthermore, a functional subtractive color filter is also designed and fabricated using this approach. The diameters of the synthesized ZnO nanorods range from 180 to 320 nm, and the subtractive color filter exhibits a wide color tuning ability from yellow to magenta to cyan. Such solution-based bottom-up fabrication of ZnO nanorods eliminates the need for dry etching, and demonstrates the potential to grow high-aspect-ratio ZnO nanostructures for efficient dielectric metasurfaces.

1. Introduction

The recent interest in artificially designed metasurfaces in the field of nanophotonics is owing to their capability to manipulate the phase, amplitude, and polarization of the incident electromagnetic waves.[1–3] A carefully designed metasurface device can fulfill similar functions as those performed by traditional bulk-optical components. In addition, it can exhibit anomalous deflection behavior that is not observed in natural bulk materials.[4–6] Based on the material used for fabrication, metasurfaces can be categorized into metallic and dielectric types.[7–9] Owing to the Mie scattering effect in dielectric materials, the oscillating electric and magnetic field displacements help in achieving full optical phase modulation along with a high transmission efficiency.[10–12] Therefore, dielectric metasurfaces have a natural advantage in designing transmissive optical devices.[13]

Among the various possible dielectric materials that are used to create high-efficiency metasurfaces, transparent conductive oxides (TCOs) have several advantages, such as a sufficiently large dielectric constant of the background environment.[14] Therefore, several high-performance dielectric metasurface devices based on metal oxides (e.g., TiO_2) have been designed and reported in the literature. For instance, Capasso and co-workers[15,16] have designed and fabricated metalenses for wavelengths 660, 532, and 405 nm using high-aspect-ratio TiO_2 nanostructures. These lenses exhibited a high working efficiency (>66%) over a broadband wavelength range while achieving a numerical aperture of 0.8 and a magnification of up to 170 times. In the work by Fan et al.,[17] a high-efficiency autofocusing airy (AFA) beam in the visible spectrum was generated using an array of amorphous TiO_2 elliptical nanorods. In addition to yielding such optical components, dielectric metasurfaces have significant potential in color display applications. High transmissive subtractive color filters with saturated structural colors based on TiO_2 or its composite have also been reported.[18–22] Thus, metal-oxide-based dielectric metasurface devices have exhibited considerable potential in several applications.

However, the fabrication of delicate nanostructures using conventional microelectronic processing is rather expensive and time-consuming, especially for metal-oxide-based materials.[18,20,21] In addition, for transmissive metasurfaces, a high aspect ratio of the unit structure is commonly required for better performance. In conventional dry etching of metal oxides, it is quite challenging to ensure a smooth sidewall and minimize lateral etching in the units.[15,23] To avoid these issues, new approaches were explored and reported by Khorasaninejad et al.,[15] which we describe here briefly. A nanostructure pattern was initially exposed by electron-beam

Dr. H. Liu, K. Li, Prof. Y. Liu, Prof. C. Qiu, Prof. Z. Liu
Department of Electrical and Electronic Engineering
Southern University of Science and Technology
Shenzhen 518055, China
E-mail: liuzj@sustech.edu.cn
D. Quan, Y. Zheng, Dr. F. Lou, Prof. G. Li, Prof. X. Cheng
Department of Materials Science and Engineering
Southern University of Science and Technology
Shenzhen 518055, China
E-mail: chengx@sustech.edu.cn
D. Quan, Prof. A. K. Srivastava
Department of Electronic and Computer Engineering
Hong Kong University of Science and Technology
Hong Kong 999077, China
Dr. S. Liu
Institute for Quantum Science and Engineering
Southern University of Science and Technology
Shenzhen 518055, China
The ORCID identification number(s) for the author(s) of this article can be found under https://doi.org/10.1002/adom.202001670.

DOI: 10.1002/adom.202001670

lithography (EBL) on an e-beam resist. The resist layer thickness was chosen to be the same as the desired height of the metasurface nanostructures. Subsequently, a thick TiO_2 layer was conformally deposited on the patterned e-beam resist layer, followed by dry etching to remove any excess layer from the top. Finally, a metalens based on this TiO_2 nanostructure array with a high aspect ratio and good sidewall quality was obtained. The success of such a fabrication approach relies on the conformality and low operational temperature in atomic layer deposition (ALD). However, the deposition rate in the ALD process is extremely slow; thus, a rather long deposition time is required to reach the desired thickness, which is at least half the maximum width of the underlying pattern.[24]

To address the challenges in the fabrication of high-aspect-ratio metal oxide nanostructures, in this work, we propose a bottom-up chemical synthesis approach using the solution-phase epitaxy (SPE) technique. We chose ZnO as the material for fabricating the metasurface in this study, the reason for which is twofold. First, the refractive index of the solution-synthesized ZnO is ≈2, which makes it transparent in the visible wavelength range.[25,26] Second, the chemical synthesis of ZnO pillars using the SPE approach has been extensively studied and reported.[27–29] To further demonstrate the feasibility of this approach, nanotoroid and nanorod arrays were rigorously tested in this work. We also fabricated a functional subtractive color filter based on ZnO nanorods. By varying the nanorod diameter and pitch, nanorod arrays of different colors were fabricated and characterized. To explore the working mechanism of these color filters, the Mie scattering behavior of the nanorods was analyzed using finite-difference time-domain (FDTD) simulations. The effects of the roughness and expanded diameter of the top segment of the ZnO nanorods were also investigated. Finally, the scattering cross-sectional efficiency of the nanorods was calculated, and the electric and magnetic multipoles were evaluated corresponding to the four resonance scattering peaks, namely, electric quadrupole (EQ), magnetic quadrupole (MQ), electric dipole (ED), and magnetic dipole (MD).

2. Experimental Section

2.1. Fabrication Process

2.1.1. Process Flow Schematic

The chemical synthesis of the ZnO nanostructures in this work is illustrated in **Figure 1**. First, a layer of ZnO was deposited on a substrate to form the seed layer, following which a poly (methyl methacrylate) (PMMA) layer was spin-coated and patterned as the sacrificial template for the growth of the ZnO nanostructures. From Figure 1 it was noted that the thickness of the PMMA layer is commensurate with the height of the ZnO metasurface. Next, EBL and development were performed. The PMMA pattern was subsequently treated with O_2 plasma to improve wettability to ensure that the ZnO seed layer was fully exposed to the precursor solution. Following this, the substrate with the patterned PMMA layer was immersed in the precursor solution, which, in fact, constitutes the SPE process. At a certain temperature, the ZnO starts to grow in the regions where the seed layer is exposed. The duration of the growth was adjusted as well as stopped manually to ensure that the height of the ZnO nanostructures matched the height of the PMMA layer. Finally, the PMMA layer was removed using a solvent such that only the ZnO nanostructures remained in the end.

2.1.2. Preparation of the Patterned Substrate

A GaN epitaxial layer with a thickness of 4.4 mm was used on a C-cut sapphire wafer (HeFei Crystal Technical Material Co., Ltd., China) as the substrate for the SPE of ZnO. A ZnO seed layer of thickness 30 nm was deposited on the substrate using ALD (PicoSun RC200, Japan). The deposition was carried out at 200 °C for 300 cycles with a flow rate of 150 sccm for diethylzinc (DEZ) and 200 sccm for H_2O. The pulse durations were 0.1 and 0.2 s for DEZ and H_2O, respectively. Note that the deposited ZnO seed layer is expected to undergo epitaxial growth on the

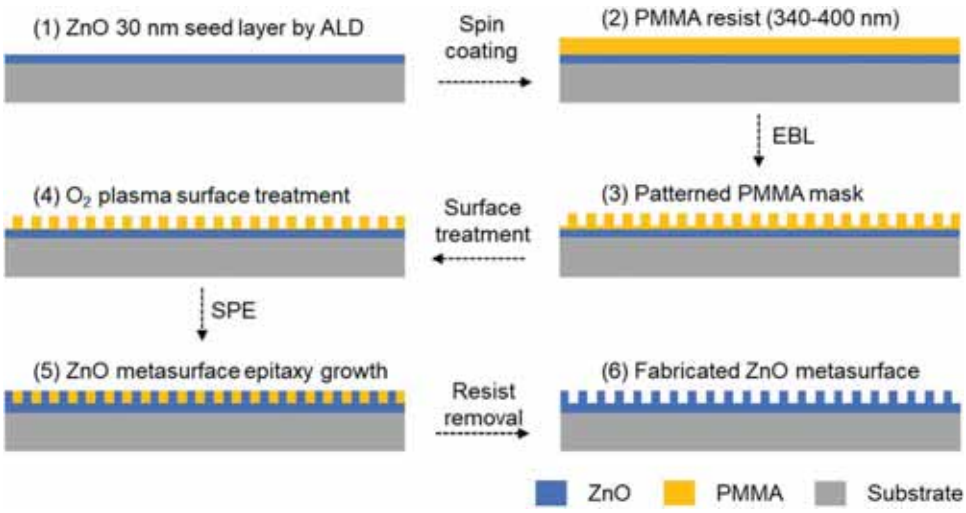

Figure 1. A schematic of the chemical synthesis of a ZnO nanostructure array in a patterned PMMA resist layer.

GaN layer due to a low lattice mismatch between the two.[30–32] A PMMA layer of thickness 420 nm was spin-coated from a 5% solution in anisole (Kayaku Advanced Materials, Japan) on top of the ZnO seed layer. The PMMA film was subsequently exposed to EBL (Elionix ELS-F125, Japan), and soaked for 60 s in a developer (Kayaku Advanced Materials, Japan) composed of methyl isobutyl ketone (MIBK) and isopropyl alcohol (IPA) with a volume ratio of 3:1. The rinsed and air-dried substrate was then treated with O_2 plasma with a power of 100 W and an O_2 flow rate of 50 sccm for 12 s to render the PMMA surface hydrophilic and to fully expose the ZnO seed layer.

2.1.3. Details of the SPE Process

The solution for the chemical bath deposition growth of ZnO nanostructures contained an equal molar ratio of $Zn(NO_3)_2$ (99.8%, Sigma Aldrich, USA) and hexamethylenetetramine (HTMA, 99.9%, Sigma Aldrich, USA), with a concentration of 0.015 M for both the components. The substrate with the patterned PMMA film was immersed in this solution with the patterned side facing down, and the reaction was conducted at 90 °C for 40–50 min in an oven. Following the growth of the ZnO nanostructures, the sample was rinsed with deionized water and dried with a gentle N_2 purge. To remove the PMMA template, the substrate was immersed in dimethyl sulfoxide (DMSO, 99.9%, Sigma Aldrich, USA) for 1 h. The pH values of the solution before and after growth were 6.2 and 5.2, respectively, which were in agreement with the corresponding values reported in the literature.[29]

2.2. Characterizations and Simulations

2.2.1. Morphological and Crystal Structure Characterizations

The roughness of the top surface of the ZnO nanorods was characterized using atomic force microscopy (AFM, Asylum Research, MFP-3D-Stand Alone, UK), the morphology of the ZnO nanorod arrays was characterized using scanning electron microscopy (SEM, Zeiss Merlin, Germany), and the crystal structure of the nanorods was evaluated using transmission electron microscopy (TEM, FEI Talos, USA).

2.2.2. Optical Characterization

The transmittance of the ZnO nanorod arrays was characterized using an integrated optical platform (CRAIC Technologies, APOLLO II, USA), in which a Xe arc lamp that generates the entire visible light spectrum (350–850 nm) was used as the illumination source. To characterize the sample properly, the transmitted light was collected through a confined window above the nanostructure array, and the background transmission was blocked using an aperture, as illustrated in Figure S1 (Supporting Information). Subsequently, the measured spectra were obtained, and the corresponding colors were evaluated using the color gamut co-ordinates in the CIE 1931 system. The thickness, refractive index (n), and extinction coefficient (k) of the ZnO film were characterized using spectroscopic ellipsometry (UVISEL, HORIBA, Japan).

2.2.3. Simulations

To design the pillar arrays and analyze the electric and magnetic field resonances in the ZnO nanostructures, FDTD simulations were carried out using Lumerical FDTD Solutions (version 2018). The height of the ZnO nanorod was fixed at 450 nm, the duty ratio (of nanorod diameter to pitch) was fixed at 0.46, and the diameter of the nanorod was swept from 170 to 350 nm.

3. Results and Discussion

3.1. ZnO Nanostructure Arrays from SPE

To validate the fabrication process of the ZnO nanostructures using SPE, different structures of nanorods and nanotoroids were grown in a precursor solution using templates of PMMA nanostructures that were patterned using EBL. The morphologies of the various nanostructures are shown in **Figure 2**. Figure 2a presents the top and side views of a nanotoroid array that was grown for 40 min, with each unit having an outer and an inner diameter of 450 and 100 nm, respectively. The height of each ring-like structure is ≈400 nm and the pitch is 660 nm. We note that the nanotoroid structures are uniform and have smooth sidewalls. The nanorods, on the other hand, were grown for 50 min to achieve a diameter of 200 nm. The morphologies of the ZnO nanorod arrays with different lattice arrangements are shown in Figure 2b,c. In Figure 2b, each cylindrical unit has a diameter 450 nm and two rectangular structures of dimension 250 nm × 450 nm. The pitch of this structure is ≈2 μm, and the overall size of the array is 50 μm × 50 μm. The dark shaded region in the topmost image of Figure 2c denotes tightly packed, vertically aligned ZnO nanorods with a few defect spots. As seen from the tilted view in the bottommost image of Figure 2c, the height and diameter of the nanorods are quite uniform, and their values are ≈798 and 270 nm, respectively (i.e., an aspect ratio of ≈3:1). The pitch of these nanorods is 585 nm.

On taking a closer look at the individual ZnO nanostructures, we clearly observe two segments for each unit (especially in Figure 2b,c): a smooth column at the bottom with a height of ≈370 nm and an uneven column at the top with a height of ≈430 nm. The bottom segment has smooth sidewalls owing to the confined growth of the ZnO within the patterned PMMA template. However, once the height of the synthesized ZnO nanorods exceeds that of the PMMA template, the growth is no longer contained in the lateral direction. This leads to uneven sidewalls as well as a slightly larger radius (≈15 nm) for the top segment of the nanorod.

In addition to sub-micrometer nanostructures, the SPE method can also fabricate ZnO patterns in the micrometer size range, as shown in Figure S2a,b (Supporting Information). The high-quality ZnO nanostructure arrays grown using SPE validate the feasibility of fabricating a ZnO metasurface using this process. Moreover, the diameter, height, and position of each rod can be strictly defined

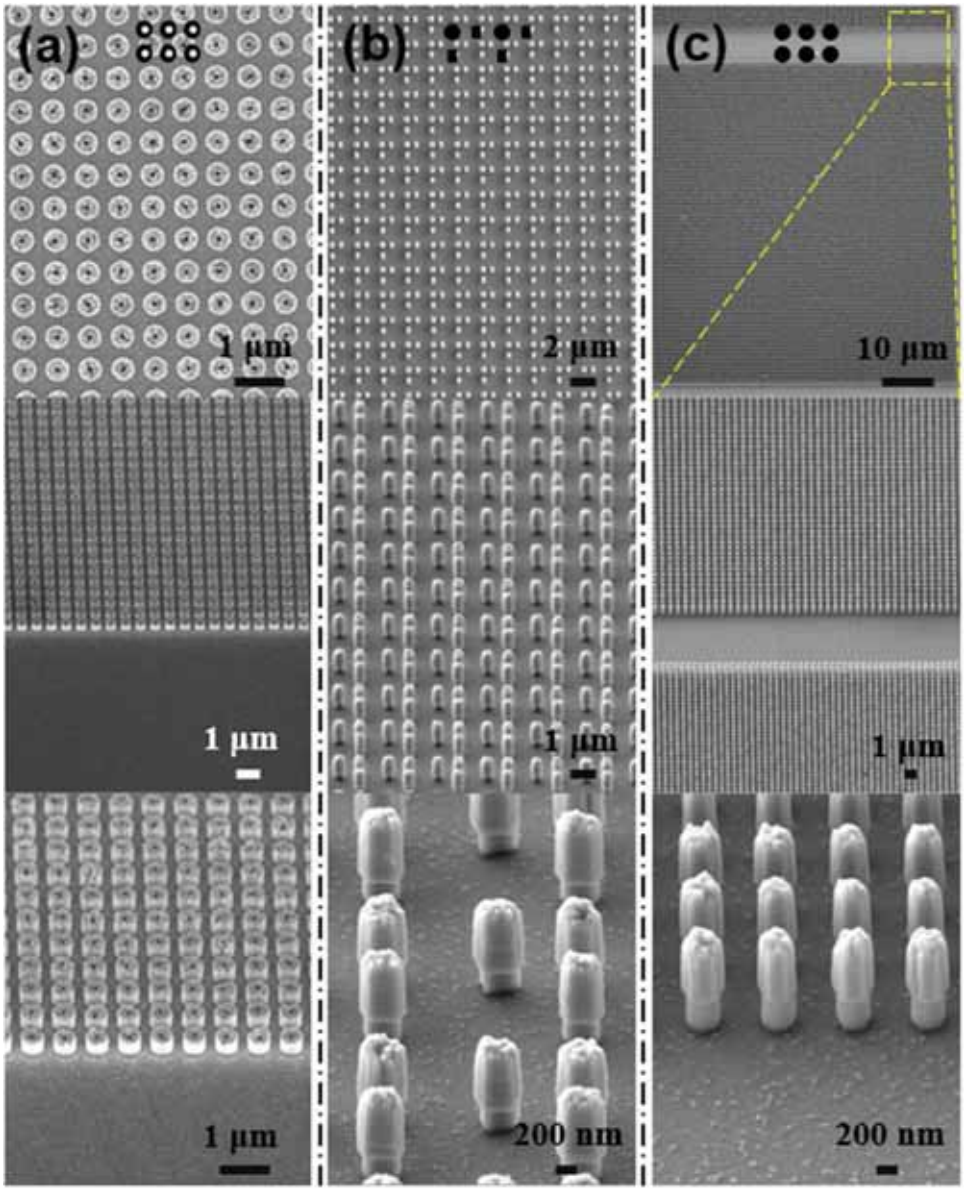

Figure 2. SEM images of the ZnO nanostructure arrays obtained using SPE. a) Nanotoroid array with an inner diameter of 100 nm, an outer diameter of 450 nm and height of 400 nm for each unit, 40 minutes growth. b,c) Nanorod arrays with height of 798 nm grown in different unit shapes and lattice arrangements for 50 minutes. The pattern displayed at the top of each image shows the lattice arrangement in the corresponding array.

by the underlying polymer template pattern. Therefore, it is extremely viable to utilize such a simple and low-cost solution process to synthesize ZnO metasurface devices in lieu of dry etching.

In previous studies, the ZnO nanorods synthesized using SPE (with heights typically in the range of 1–2 μm) were generally single crystals.[28,29] These studies used a very thin PMMA layer (≈100 nm) such that the confined growth of the ZnO within the PMMA template had much less impact on the structure of the resulting nanorods. By contrast, the PMMA template used in our work is much thicker; thus, the impact of the confined growth of the ZnO on the crystal structure of the nanorods needs to be studied by TEM.

To perform TEM characterization, ZnO nanorods were grown for 30 min at a temperature of 90 °C. The TEM images of these nanorods are shown in **Figure 3**. Figure 3a shows several ZnO nanorods that were scratched off from the substrate after the completion of the SPE process. The nanorod seen at the center of the field of view is ≈150 nm in diameter and 262 nm in length. The flat end of this nanorod is in fact the bottom segment that is in contact with the substrate during SPE, whereas the other end with an irregular surface is the top segment. The lattice orientations in these two segments were carefully examined: one region was selected from the edge of the sidewall (Figure 3b) and another from the top surface of the nanorod (Figure 3c). For both these regions, the orientation of the lattice planes is observed to be along the [0001] direction, which indicates the preferential direction of growth of the ZnO nanorod.

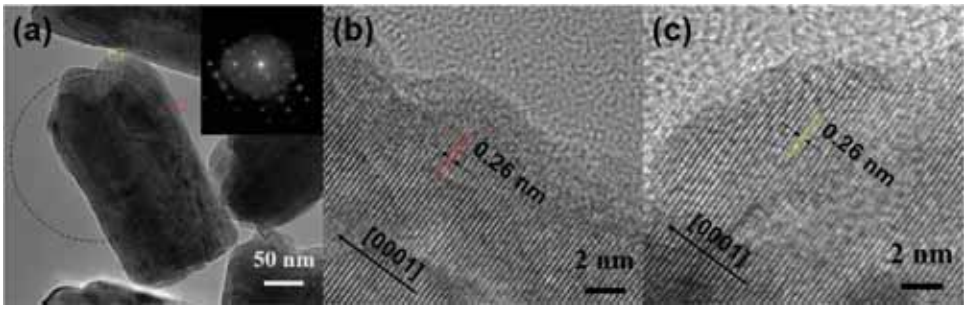

Figure 3. TEM analysis of ZnO nanorods grown within a patterned PMMA template. a) General view of a few ZnO nanorods scratched off from the array, with the inset showing the selective area electron diffraction (SAED) pattern inside the black dashed circle. b) Grain orientation in the sidewall of the ZnO nanorod as indicated by the red lines. c) Grain orientation in the top surface of the ZnO nanorod as indicated by the yellow lines.

This is expected considering that the same [0001] orientation was also used for the GaN/sapphire substrate. Note that the spacing between the adjacent lattice planes is ≈0.26 nm, which is close to the reported values for the wurtzite structure of ZnO.[33–35] To obtain the crystal structure of this nanorod, selective area electron diffraction (SAED) was conducted within the region enclosed by the black dashed circle in Figure 3a. We note that the characterization region covers the majority of the nanorod, and thus, the diffraction pattern in the inset of Figure 3a implies that the grown nanorod is most likely a single crystal.

3.2. Optical Properties of ZnO Films

The optical properties (e.g., *n* and *k* values) of the ZnO structures depend on the growth or deposition methods.[36–40] Therefore, an accurate measurement of the *n* and *k* values of the ZnO film prepared by SPE is essential to facilitate the design of a functional metasurface device. For comparison, the *n* and *k* values of both the ZnO seed layer and the ZnO film obtained by SPE were characterized by using a spectroscopic ellipsometer. By fitting the measured data, the *n* and *k* dispersion curves were obtained, as shown in **Figure 4**.

Figure 4a presents the *n* and *k* dispersion curves in the visible spectrum range of the ZnO seed-layer film obtained using ALD. We see that the *n* value varies significantly from 2.25 at 400 nm to 1.4 at 800 nm, whereas the *k* value remains close to 0 across the entire wavelength range. Figure 4b presents the dispersion curves of a ZnO film that was deposited using SPE at 90 °C for 20 min, with a ZnO seed layer/GaN epitaxy layer/Al_2O_3-*c* (0001) as the substrate. The thickness of this film as measured by ellipsometry is ≈46.4 nm. We observe that the surface of this film is quite smooth (see the inset of Figure 4b). Note that the effect of the ZnO seed layer was excluded from the SPE data by using the seed layer in Figure 4a as the substrate model. We observe that the fitted *n* value of the ZnO obtained by SPE changes from 2.65 at 400 nm to 1.83 at 800 nm, which is in accordance with the values reported in the literature.[41,42] In addition, unlike the ZnO film deposited by ALD, the ZnO film deposited by SPE exhibits a rather high extinction coefficient of 0.5 that decreases rapidly to a near-zero value in the wavelength range 400–450 nm. Such a behavior is commonly associated with lattice defects.[39,40,43]

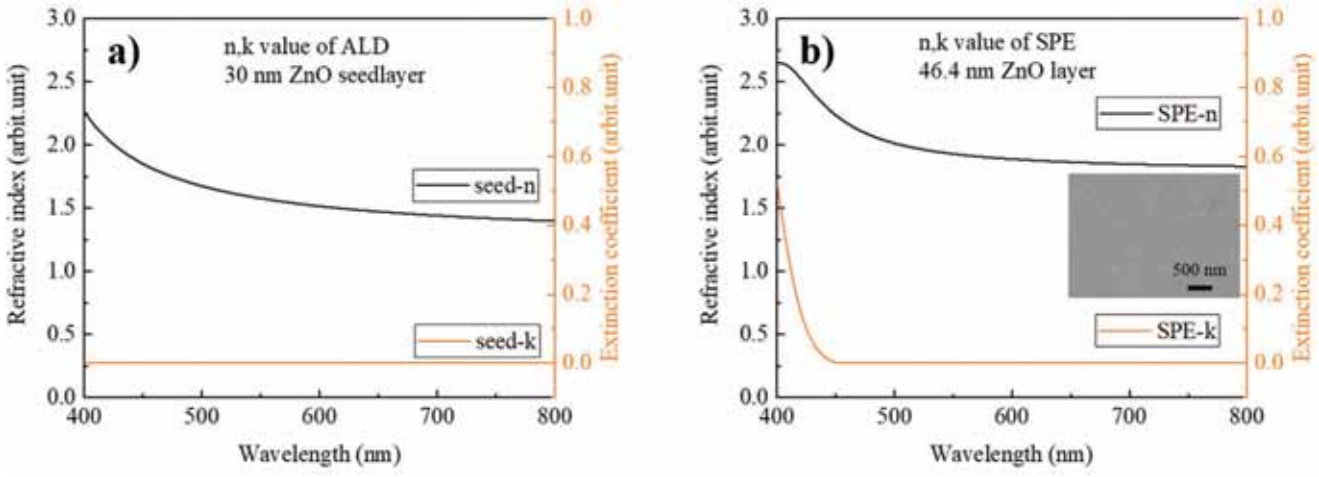

Figure 4. The *n* and *k* dispersion curves of a) 30 nm ZnO seed-layer film deposited by ALD, and b) 46.4 nm ZnO film deposited by SPE. The inset in panel (b) shows an SEM image of the surface morphology of the ZnO film.

3.3. Design, Characterization, and Analysis of Subtractive Color Filters

In our FDTD simulations, the diameter of the nanorods was swept from 170 to 350 nm with a duty ratio fixed at 0.46. The parameter sweeping map is presented in **Figure 5**. Figure 5a shows the variation of the transmission spectrum with the nanorod diameter. In Figure 5b, the transmission spectra of selected nanorods having diameters in the range of 177–317 nm are presented.

Figure 6 shows a 45° tilted view of ZnO nanorods having different diameters obtained after 40 min of growth in a chemical bath at 90 °C. The measured diameters of the ZnO nanorods were found to be very close to the desired parameters, and the small differences can be attributed to the EBL process. As shown in the inset of Figure 6a, the array of ZnO nanorods with a diameter of 178 nm produces a light yellow color under an optical microscope with illumination from the bottom. The SEM image of the ZnO nanostructure shows that each rod contains two sections: a smooth bottom segment and an uneven top segment with a slightly larger diameter (≈15 nm). Note that the height of the bottom segment is similar to that of the PMMA resist pattern (≈400 nm), whereas the height of the top segment is ≈37 nm.

The roughness of the sidewall of the bottom segment of the ZnO nanorod is similar to that of the PMMA sidewall, which has an RMS roughness of ≈2 nm.[23] By increasing the diameter of the ZnO nanorod from 198 to 276 nm, the color produced by these arrays changes from dark yellow to blue, as shown in the insets of Figure 6b–g. We observe that the colors produced by the nanorod arrays in Figure 6a–g are relatively uniform across the square patch. However, for ZnO nanorods with even larger diameters of 285 and 322 nm, the optical images start to present a mixture of green, blue, and cyan colors, as seen in Figure 6h,i. The color in these two cases does not appear to be as uniform as in the cases with smaller nanorod diameters. From the 45° tilted view, we also observe that the top segments of the ZnO nanorods in Figure 6h,i are significantly longer than in the other cases. In addition, we note that the height of the ZnO nanorods varies slightly with the location in the array. This is possibly due to fluctuations in the precursor concentration during the growth process.

In general, the diameter and position of the ZnO nanorods can be precisely controlled by PMMA patterning. In the subtractive color filters designed and fabricated in this work, the color evolves from yellow to magenta and eventually to cyan. The colors produced by the ZnO arrays are clear and saturated, indicating a high sidewall quality and low defect rate in the ZnO nanorods. The top-down views of these arrays are provided in Figure S3 (Supporting Information). We observe from Figure 3a–i that the diameters of the ZnO nanorods in the array are quite uniform. This uniform distribution of the diameters is further illustrated in Figure S3j (Supporting Information).

The transmission spectrum of each array was measured using a CRAIC optical characterization microscope, and the results are presented in **Figure 7**a. We observe that there is always a dip present in the transmission intensity spectrum at a certain wavelength for all nanorod diameters. This is because the designed metasurface device functions as a subtractive color filter. Furthermore, this dip in transmittance shifts to longer wavelengths with larger nanorod diameters; thus, the color of each ZnO array evolves with the nanorod diameter to provide a wide range of color tuning abilities. For the arrays with nanorod diameters ranging from 276 to 322 nm, a second dip in the transmittance appears in the corresponding spectra at a lower wavelength of ≈450 nm, which can be associated with the Fabry–Pérot resonance in the nanorod structures.[18,19] We observe that for most wavelengths in the transmission spectra, the off-resonance transmission efficiency is ≈70%. Considering that the transmission efficiency of the substrate is only ≈80–84% in the visible spectrum (as shown in Figure S4 in the Supporting Information), the working efficiency of our color filters is thus reasonable.

The color coordinates of the measured and simulated spectra (from Figure 4b) are plotted for comparison in the color gamut in Figure 7b using the CIE 1931 standard. We observe that the simulated and measured coordinates lie quite close to each other. The simulated transmission spectra of the arrays with the three main colors—yellow, magenta, and cyan—are compared with the corresponding measured spectra in Figure 7c. We observe that the position of the dip in transmittance for all three colors agrees well between the simulated and measured spectra. However, a broadening of the dip is observed in the measured spectra, especially for the color cyan. The differences

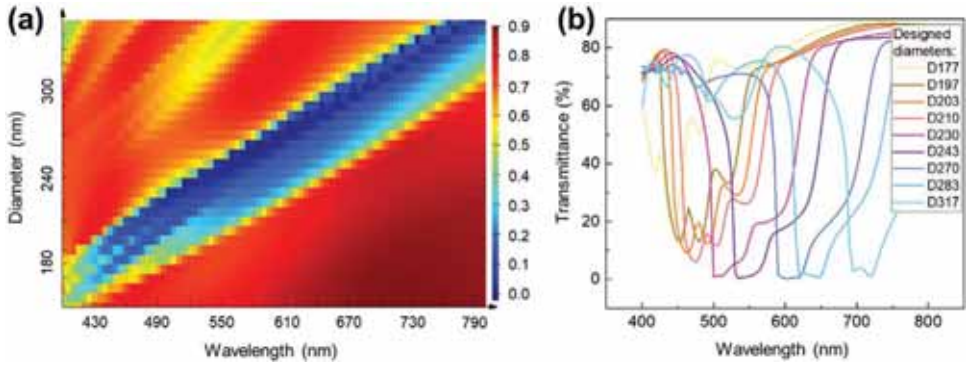

Figure 5. FDTD calculations for the design of the subtractive color filter. a) Transmission spectral map obtained by sweeping across the ZnO nanorod diameter. b) Transmission spectra for a range of nanorod diameters selected for fabrication. The duty ratio and height of the nanorods were fixed at 0.46 and 450 nm, respectively.

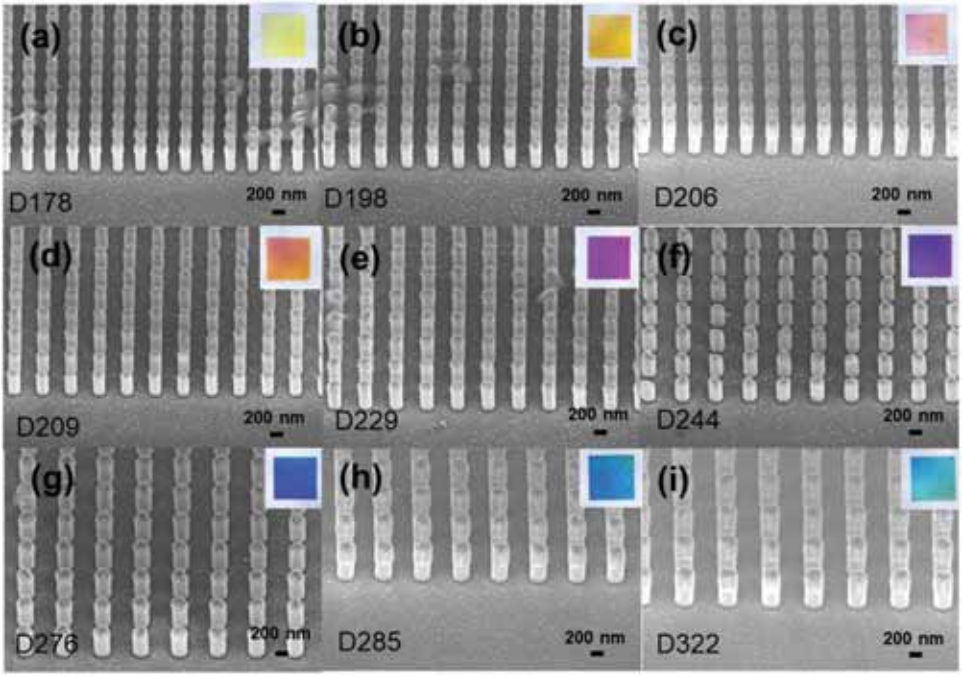

Figure 6. SEM images of a 45° tilted view of subtractive color filters composed of ZnO nanorods with diameters: a) 178 nm, b) 198 nm, c) 205 nm, d) 210 nm, e) 229 nm, f) 244 nm, g) 276 nm, h) 285 nm, and i) 322 nm. The samples were grown in a 0.015 M precursor solution at 90 °C for 40 min.

in the simulated and measured spectra can be attributed to the top segment of the ZnO nanostructure, which we discuss, in detail, in the following sections.

During the synthesis of ZnO nanorods in a chemical solution, an uneven top surface is almost inevitable compared with other thin-film deposition techniques. A systematic study has showed that the sidewall roughness of the nanorods in the dielectric metasurface plays a significant role in the metasurface performance.[23] In our method, the nanorod sidewall roughness is determined by the roughness of the PMMA resist because the ZnO growth is confined within the polymer template. Therefore, it is the roughness of the top surface of the nanorod that is of primary concern in this study, which we investigated using FDTD simulations.

By considering the magenta color filter (corresponding to a nanorod with a diameter of 230 nm) as an example, we analyzed the effects of the roughness and diameter of the overgrown top surface of the nanorod on the transmission spectra using FDTD simulations, as shown in **Figure 8**. The pitch was set to be 500 nm, the height (h_{top}) of the top segment that exceeded the PMMA resist was fixed at 80 nm, and the total height of the ZnO nanostructure was fixed at 450 nm. The parameter R_{plus} is defined in the inset of Figure 8b, which describes the amount by which the radius of the top segment exceeds than that of the bottom segment. With the correlation length of the surface roughness fixed at 15 nm, we simulated the transmission spectra of the ZnO nanostructure by increasing the RMS roughness from 0 to 30 nm for an R_{plus} value of 0, as shown in Figure 8a. The nearly identical spectra show that the position of the dip in transmittance as well as the off-resonance transmission efficiency are minimally impacted by the roughness of the top surface of the ZnO nanostructures. The average roughness of the top surface was measured to be ≈18 nm using AFM. Thus, we can conclude that the surface roughness of the ZnO nanorods fabricated by SPE has negligible influence on the performance of the corresponding metasurface color filters.

In addition to the top surface roughness, the effect of the expanded radius of the top segment of the nanorods was investigated. As shown in Figure 8b, we varied R_{plus} from 0 to 30 nm in our FDTD simulations with an RMS top surface roughness fixed at 18 nm. We observe that the transmittance in the wavelength range 550–600 nm increases with increasing R_{plus}, which is consistent with the greenish color of the ZnO nanostructures with large overgrown top segments (see Figure 6i).

To understand the working mechanism behind the subtractive color filters, the scattering cross-sectional efficiency of the ZnO nanorod arrays was calculated, and the underlying resonant electric and magnetic fields were examined. Again, we used the ZnO nanorods with a diameter of 229 nm (i.e., magenta color) as an example, whose simulated transmission spectrum is shown in Figure 7c. To reveal the structural effects of the nanorods on the scattering resonance, nanorods with different configurations are compared in **Figure 9**a. We observe that the scattering cross-sectional curves of the ZnO nanorods with top surface RMS roughness values of 18 nm (solid black line) and 0 nm (red dashed line) almost coincide with each other. This confirms the results shown in Figure 8a that the top surface roughness has a little effect on the electric and magnetic fields at resonance, and hence on the transmission spectra. However, the excess radius R_{plus} of the top segment of the ZnO nanorods indeed has a significant impact on the resonance wavelength. We observe that all the four peaks in the scattering cross-sectional curve undergo a redshift when R_{plus} increases to 30 nm (solid blue line).

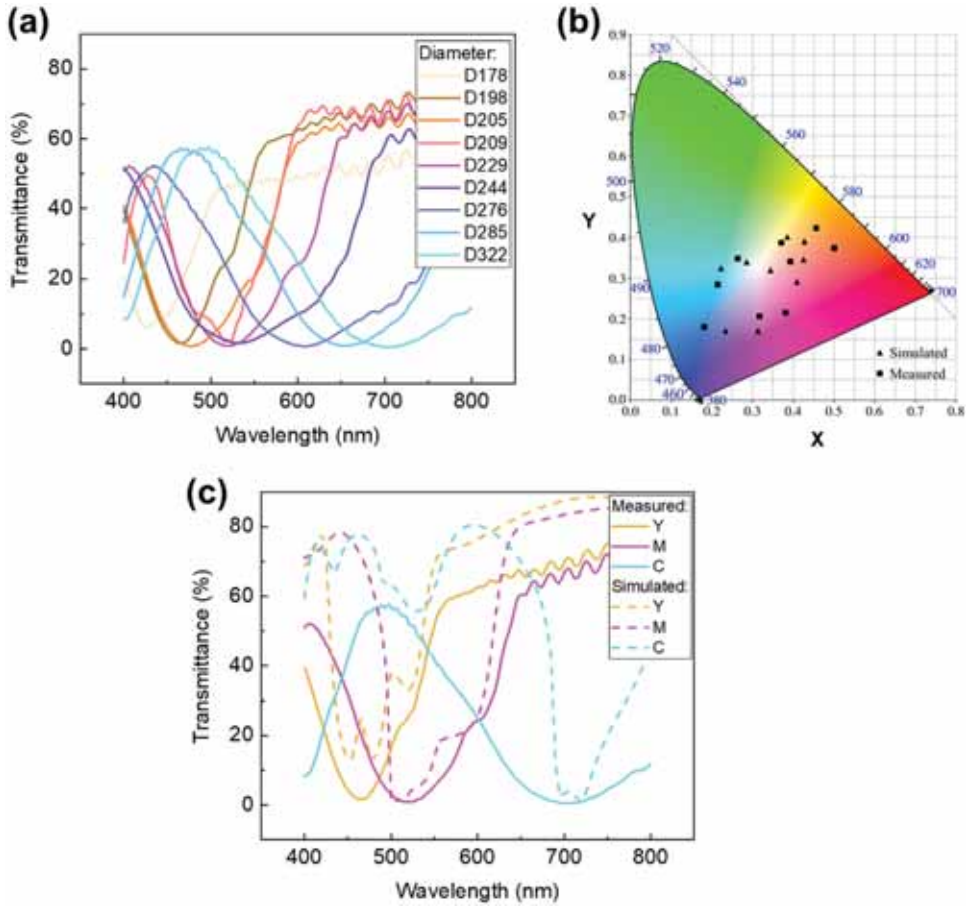

Figure 7. Optical characterization and analysis of ZnO nanorod arrays. a) Measured transmission spectra of nanorods with different diameters. b) Comparison of the simulated and measured color coordinates in a color gamut (CIE 1931). c) Comparison of the simulated and measured transmission spectra for yellow, magenta, and cyan colors.

In all the simulated cases of Figure 9a, four scattering resonant peaks are observed. For R_{plus} = 0 nm, the four resonant peaks are located at 495, 520, 555, and 620 nm, corresponding to the EQ, MQ, ED, and MD modes, respectively. The electric (*E*) and magnetic (*H*) field profiles in the *XZ*- and *YZ*-planes corresponding to these four peaks are presented and analyzed in Figure 9b–e. The EQ mode at 495 nm (Figure 9b) can be recognized by the two reinforced *E*-field centers, and the current loops in the *H*-field in the *YZ*-plane cross section of the ZnO nanorod. The MQ mode at 520 nm (Figure 9c) can be identified by the two reinforced *H*-field centers along with the two charge displacement loops in the *XZ*-plane cross section of the nanorod. The ED mode at 555 nm (Figure 9d) is signified by an enhanced *E*-field center associated with a corresponding

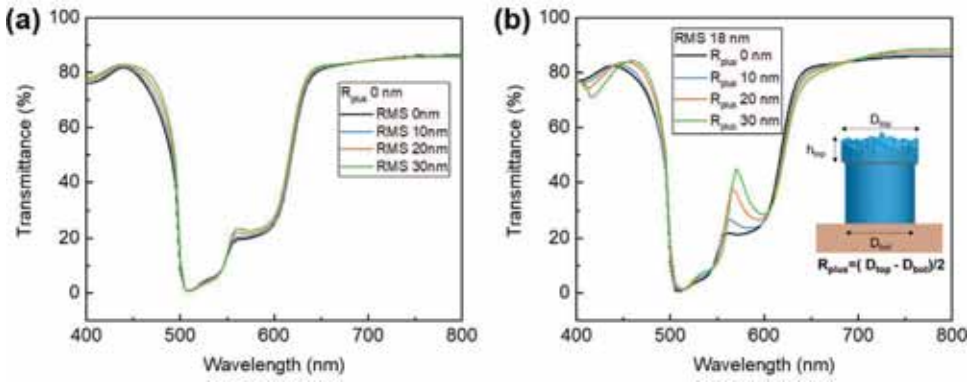

Figure 8. FDTD analysis of the effect of various properties of the ZnO nanostructures on the transmission spectra: a) top surface roughness and b) top segment diameter.

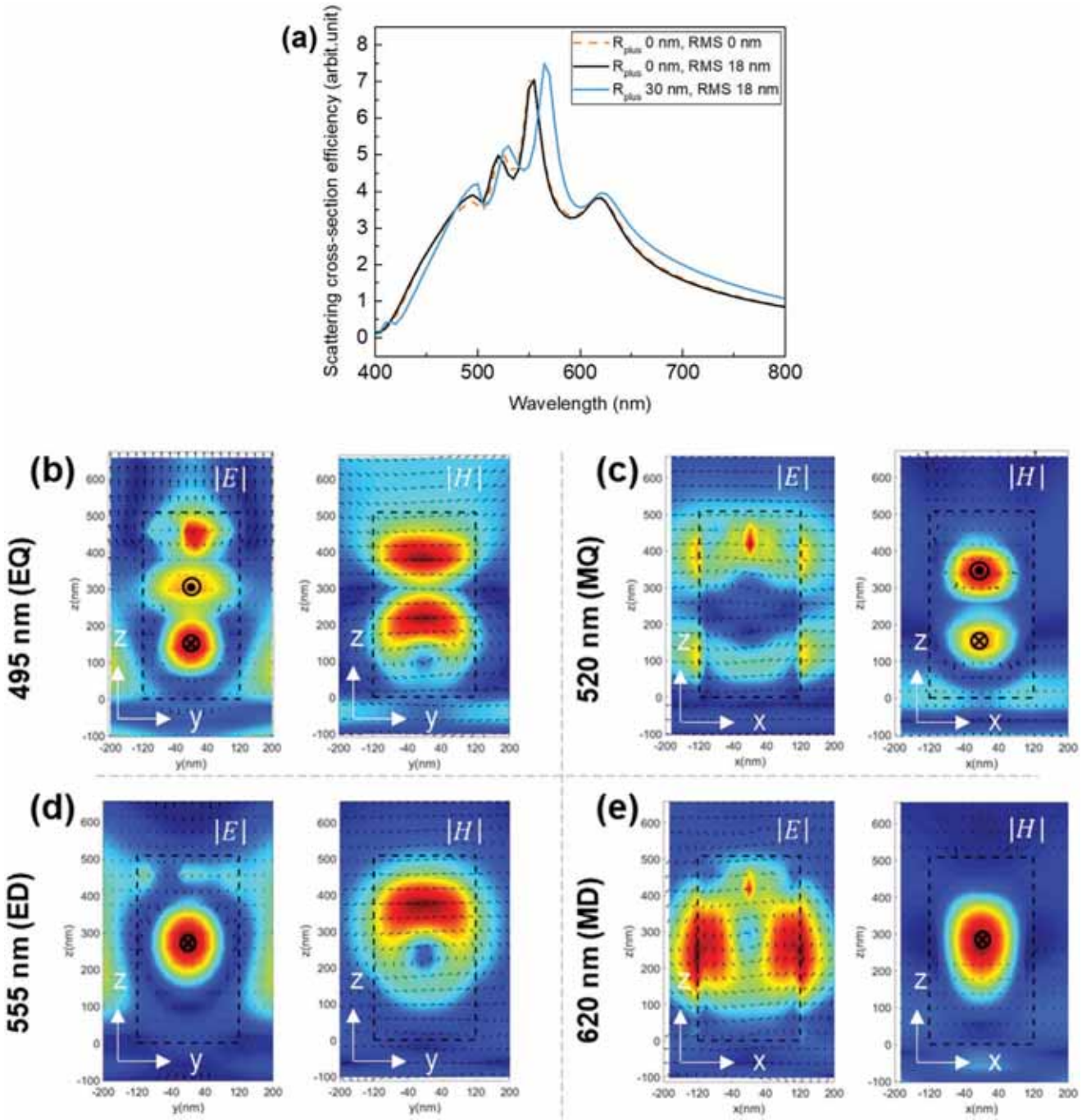

Figure 9. Analysis of the scattering cross sections and the corresponding electromagnetic field distributions in the ZnO nanorods. a) The simulated scattering cross-sectional efficiency of a ZnO array with nanorod diameter, total nanorod height, and excess top segment radius (R_{plus}) of 229, 450, and 0 nm, respectively. b–e) The corresponding electric and magnetic field distributions represent the modes: b) EQ at 495 nm, c) MQ at 520 nm, d) ED at 555 nm, and e) MD at 620 nm. The rectangular dashed line outlines the cross section of the ZnO nanorod.

current loop in the *H*-field in the *YZ*-plane cross section of the nanorod. Finally, the MD mode at 620 nm (Figure 9e) is marked by an enhanced *H*-field center with a circular charge displacement in the *E*-field in the *XZ*-plane cross section of the nanorod. Note that the rectangular dashed line in the images outlines the nanorod, and the interface between the nanorod and the substrate lies in the *XY* horizontal plane.

4. Conclusion

In this work, we proposed the fabrication of a dielectric metasurface using SPE of ZnO in polymer templates. This new fabrication scheme eliminates the need for conventional thin-film deposition and dry etching processes. To validate the feasibility of our method, arrays of ZnO toroids and rods with

diameters of 100 nm were synthesized. The sidewall of the ZnO nanostructures is perpendicular to the substrate and has a low surface roughness owing to the PMMA confinement. Based on the proposed process, metasurface color filter devices were also designed and fabricated, as the diameter and pitch of the nanorods in the array can be precisely controlled by the lithographic process. We found that the chemically synthesized subtractive color filters exhibit a reasonable off-resonance transmission efficiency of ≈70% for most of the visible wavelength range. The wavelengths corresponding to the dip in transmission intensity of these filters evolve with the design parameters such that the three basic colors—yellow, magenta, and cyan—could be achieved. Our FDTD simulations revealed that the top surface roughness of the nanorods has limited impact on the general transmission spectra of the devices. Meanwhile, for the nanorods with an overgrown top segment, its expanded radius introduces a significant redshift in the transmission spectrum. Finally, the scattering cross section of the nanorods was analyzed to understand the working mechanism of the color filters. From our simulations, we found that a top segment with an R_{plus} of 30 nm redshifts the entire scattering cross-sectional curve. By observing the electric and magnetic fields at the four resonant peaks of the scattering cross-sectional curve, we identified all the resonant modes corresponding to different multipoles. We found that the ED mode was the most dominant resonant mode for the corresponding nanorod structure. The emergence of the multipoles in the electromagnetic field distribution explains the broadening of the dip in the transmission spectra of the nanorod arrays.

Overall, we conclude that a ZnO metasurface device with a high aspect ratio can be synthesized using solution-phase epitaxial growth in a prepatterned polymer template. Compared with the conventional top-down fabrication approach, this bottom-up fabrication scheme is less time-consuming, less expensive, and more scalable. Furthermore, lateral etching and sidewall roughness as a result of plasma etching in conventional top-down fabrication methods are detrimental for most metasurface applications, whereas, these issues are not present in our bottom-up fabrication method. Although issues such as the uneven top surface of the ZnO nanorods still need to be addressed, SPE of metal oxide nanostructures offers a facile and viable fabrication method for dielectric metasurfaces that can be used for a wide range of applications.

Supporting Information

Supporting Information is available from the Wiley Online Library or from the author.

Acknowledgements

H.L. and D.Q. contributed equally to this work. H.L. acknowledges the funding support from the Liquid Crystal Waveguiding Research Program (Grant No. YBN2018035208). C.Q. thanks the International Technology Cooperation Program (Grant No. 2018A050506002) for financial support. This work was supported by the Shenzhen Science and Technology Innovation Committee for Basic Science (Grant No. JCYJ20160301114303878). EBL exposures were carried out with support from the Institute for Quantum Science and Engineering at SUSTech with the help of Hao Jia. The authors acknowledge the assistance of the SUSTech Core Research Facilities and the technical support from Xuhang Ma.

Conflict of Interest

The authors declare no conflict of interest.

Keywords

dielectric metasurfaces, solution-phase epitaxy, subtractive color filters, ZnO nanorods

Received: September 26, 2020
Revised: November 22, 2020
Published online: December 23, 2020

[1] Q. He, S. Sun, S. Xiao, L. Zhou, *Adv. Opt. Mater.* **2018**, *6*, 1800415.
[2] H. T. Chen, A. J. Taylor, N. Yu, *Rep. Prog. Phys.* **2016**, *79*, 076401.
[3] M. K. Keshavarz Hedayati, M. Elbahri, *Plasmonics* **2017**, *12*, 1463.
[4] H. Shi, J. Li, A. Zhang, Y. Jiang, J. Wang, Z. Xu, S. Xia, *IEEE Antennas Wireless Propag. Lett.* **2015**, *14*, 104.
[5] J. X. Cao, X. J. Zhang, D. Q. Geng, *J. Clin. Neurol.* **2010**, *23*, 414.
[6] H. J. Lezec, A. Degiron, E. Devaux, R. A. Linke, L. Martin-Moreno, F. J. Garcia-Vidal, T. W. Ebbesen, *Science* **2002**, *297*, 820.
[7] H.-H. Hsiao, C. H. Chu, D. P. Tsai, *Small Methods* **2017**, *1*, 1600064.
[8] N. M. Estakhri, A. Alù, *J. Opt. Soc. Am. B* **2016**, *33*, A21.
[9] A. Li, S. Singh, D. Sievenpiper, *Nanophotonics* **2018**, *7*, 989.
[10] A. I. Kuznetsov, A. E. Miroshnichenko, M. L. Brongersma, Y. S. Kivshar, B. Luk'yanchuk, *Science* **2016**, *354*, aag2472.
[11] J. A. Schuller, R. Zia, T. Taubner, M. L. Brongersma, *Phys. Rev. Lett.* **2007**, *99*, 107401.
[12] Y. H. Fu, A. I. Kuznetsov, A. E. Miroshnichenko, Y. F. Yu, B. Luk'yanchuk, *Nat. Commun.* **2013**, *4*, 1527.
[13] P. Genevet, F. Capasso, F. Aieta, M. Khorasaninejad, R. Devlin, *Optica* **2017**, *4*, 139.
[14] J. Yang, J. A. Fan, *Opt. Express* **2017**, *25*, 23899.
[15] M. Khorasaninejad, W. T. Chen, R. C. Devlin, J. Oh, A. Y. Zhu, F. Capasso, *Science* **2016**, *352*, 1190.
[16] M. Khorasaninejad, W. T. Chen, A. Y. Zhu, J. Oh, R. C. Devlin, C. Roques-Carmes, I. Mishra, F. Capasso, *IEEE J. Sel. Topics Quantum Electron.* **2017**, *23*, 43.
[17] Q. Fan, D. Wang, P. Huo, Z. Zhang, Y. Liang, T. Xu, *Opt. Express* **2017**, *25*, 9285.
[18] I. Koirala, S. S. Lee, D. Y. Choi, *Opt. Express* **2018**, *26*, 18320.
[19] B. Yang, W. Liu, Z. Li, H. Cheng, D. Y. Choi, S. Chen, J. Tian, *Nano Lett.* **2019**, *19*, 4221.
[20] S. Sun, Z. Zhou, Z. Duan, S. Xiao, Q. Song, *ACS Nano* **2017**, *11*, 4445.
[21] Y. Huang, H. Xu, Y. Lu, Y. Chen, *J. Phys. Chem. C* **2018**, *122*, 2990.
[22] Y. Wu, W. Yang, Y. Fan, Q. Song, S. Xiao, *Sci. Adv.* **2019**, *5*, eaax0939.
[23] H. Yang, H. Liu, B. Song, Y. Li, D. Meng, B. Chen, P. Hu, Y. Wang, T.-H. Ou, M. L. Povinelli, W. Wu, *Nanophotonics* **2020**, *9*, 1401.
[24] J. P. Niemelä, G. Marin, M. Karppinen, *Semicond. Sci. Technol.* **2017**, *32*, 093005.
[25] C. C. Ting, S. P. Chang, *Adv. Mater. Res.* **2011**, *225*, 597.
[26] P. B. Taunk, R. Das, D. P. Bisen, R. K. Tamrakar, N. Rathor, *Karbala Int. J. Mod. Sci.* **2015**, *1*, 159.
[27] A. Qurashi, J. H. Kim, Y. B. Hahn, *Superlattices Microstruct.* **2010**, *48*, 162.

[28] V. Consonni, E. Sarigiannidou, E. Appert, A. Bocheux, S. Guillemin, F. Donatini, I. C. Robin, J. Kioseoglou, F. Robaut, *ACS Nano* **2014**, *8*, 4761.
[29] T. Cossuet, E. Appert, J. L. Thomassin, V. Consonni, *Langmuir* **2017**, *33*, 6269.
[30] J. Volk, R. Erdélyi, *Turk. J. Phys.* **2014**, *38*, 391.
[31] Z. Baji, Z. Lábadi, Z. E. Horváth, G. Molnár, J. Volk, I. Bársony, P. Barna, *Cryst. Growth Des.* **2012**, *12*, 5615.
[32] Z. Baji, Z. Lábadi, G. Molnár, B. Pécz, K. Vad, Z. E. Horváth, P. J. Szabó, T. Nagata, J. Volk, *Thin Solid Films* **2014**, *562*, 485.
[33] R. Ghosh, S. Kundu, R. Majumder, S. Roy, S. Das, A. Banerjee, U. Guria, M. Banerjee, M. K. Bera, K. M. Subhedar, M. P. Chowdhury, *Appl. Nanosci.* **1939**, *9*, 2019.
[34] X. Liu, L. Ye, S. Liu, Y. Li, X. Ji, *Sci. Rep.* **2016**, *6*, 38474.
[35] X. Huang, M. G. Willinger, H. Fan, Z. L. Xie, L. Wang, A. Klein-Hoffmann, F. Girgsdies, C. S. Lee, X. M. Meng, *Nanoscale* **2014**, *6*, 8787.
[36] N. Hamzaoui, A. Boukhachem, M. Ghamnia, C. Fauquet, *Results Phys.* **1950**, *7*, 2017.
[37] A. El-Yadouni, A. Boudrioua, J. C. Loulergue, V. Sallet, R. Triboulet, *Opt. Mater.* **2005**, *27*, 1391.
[38] A. Bedia, F. Z. Bedia, M. Aillerie, N. Maloufi, B. Benyoucef, *Energy Procedia* **2014**, *50*, 603.
[39] A. E. l. Hamidi, K. Meziane, A. E. l. Hichou, T. Jannane, A. Liba, J. E. l. Haskouri, P. Amorós, A. Almaggoussi, *Optik* **2018**, *158*, 1139.
[40] S. Sharma, C. Periasamy, P. Chakrabarti, *Electron. Mater. Lett.* **2015**, *11*, 1093.
[41] F. Baig, A. Asif, M. W. Ashraf, M. Imran, *Mater. Res. Express* **2020**, *7*, 026417.
[42] S. Kumar, H. C. Jeon, T. W. Kang, R. Seth, S. Panwar, S. K. Shinde, D. P. Waghmode, R. G. Saratale, R. K. Choubey, *J. Mater. Sci.: Mater. Electron.* **2019**, *30*, 17747.
[43] C. Manoharan, G. Pavithra, M. Bououdina, S. Dhanapandian, P. Dhamodharan, *Appl. Nanosci.* **2016**, *6*, 815.